



Synergizing electron transfer with singlet oxygen to expedite refractory contaminant mineralization in peroxymonosulfate based heterogeneous oxidation system

Yun-Xin Huang^b, Ke-Yu Chen^b, Shi-Xu Wang^b, Shou-Yan Zhao^b, Lin-Qian Yu^b, Bao-Cheng Huang^{a,b,*}, Ren-Cun Jin^{a,b}

^a School of Engineering, Hangzhou Normal University, Hangzhou 310018, China

^b School of Life and Environmental Sciences, Hangzhou Normal University, Hangzhou 311121, China

ARTICLE INFO

Keywords:

Peroxymonosulfate
Non-radical oxidation
Electron transfer pathway
Singlet oxygen
Wastewater treatment

ABSTRACT

This work explored the feasibility of synergizing singlet oxygen ($^1\text{O}_2$) and electron transfer pathway (ETP) during catalytic decomposition of peroxymonosulfate to advance the refractory pollutant mineralization. N doping strategy was employed to synthesize Mn-C-N catalyst with two independent catalytic sites. The results showed that the contribution of $^1\text{O}_2$ and ETP to diclofenac removal could be well matched to 56% and 44% in Mn-C-N/PMS oxidation system, respectively. Mechanism studies revealed that $^1\text{O}_2$ would generate intermediate products with low E_{LUMO} , which were rapidly transformed via ETP and finally resulted in improved mineralization performance. Under 0.2 g/L Mn-C-N, 50 mg/L diclofenac, 0.4 g/L peroxymonosulfate, and actual water quality conditions, about 100% removal (15 min) and 70% mineralization efficiency (1 h) was achieved. The above non-radical oxidation system was effective for treating livestock wastewater and secondary effluent. This work prospects the synergy of non-radicals for remediating refractory contaminants-laden wastewater.

1. Introduction

Refractory organic pollutants have gained intense attention in the past few decades, due to their potential adverse impact on human and wildlife health. Ring opening and mineralization of these contaminants by oxidative species are one of the commonly employed remediation strategies. Recently, the persulfate-based advanced oxidation process has shown a great potential for removal of refractory organic pollutants, by taking into account of several attractive merits [1]. Upon the activation of persulfate with either catalyst or external energy, oxidative species with a high redox potential, i.e., hydroxyl radicals ($\cdot\text{OH}$, $E^0 = 1.9 - 2.7 \text{ V}_{\text{NHE}}$) and sulfate radicals ($\text{SO}_4\cdot$, $E^0 = 2.6 - 3.1 \text{ V}_{\text{NHE}}$) [2], can then be produced [3]. Although radicals are efficient in mineralizing organics into CO_2 and H_2O , they are easily affected and probably annihilated by solute components, inorganic ions, and even pH fluctuations [4,5], which in turn increases the invalid consumption of oxidants. Consequently, there is an urgent need to improve the effective utilization efficiency of persulfate, thereby reducing operation costs while improving the sustainability of wastewater remediation process.

Besides radical regime, it has been widely reported that persulfate would also dissociate via non-radical pathway, i.e., electron transfer process (ETP) [6], singlet oxygen ($^1\text{O}_2$) [7], and high-valent metal-oxo species [8], during heterogeneously catalytic degradation of pollutants. The above non-radical oxidation processes have been observed on various catalysts such as single atom catalyst [7], nano-carbon material [9], and metal oxides [2], etc. Compared with radicals, non-radicals have the advantages of higher selectivity for electron-rich organic pollutants and higher catalytic efficiency in complex wastewater matrix [10], which can effectively address the invalid consumption of oxidative species by interfere substances. The aforementioned property endows non-radical oxidation process with a decreased persulfate consumption amount. From this point of view, non-radical oxidation sheds a bright light on promoting the sustainability of advanced oxidation technology which is currently intensely chemicals dependent. However, due to the low redox potential of non-radical species such as ETP [11], their mineralization ability towards pollutants is poor. Improving the treatment efficiency of non-radical oxidation process is thus of great significance for its potential application in remediation of refractory

* Corresponding author at: School of Engineering, Hangzhou Normal University, Hangzhou 310018, China.

E-mail address: huangbc@hznu.edu.cn (B.-C. Huang).

¹ ORCID: 0000-0001-7074-4089

pollutants-laden wastewater.

Previous studies have shown that the molecular structure of pollutants played a pivotal role in determining reaction mechanism [12]. For instance, it is feasible to degrade pollutants with low ionization potentials by ETP while pollutants with high ionization potentials are difficult to donate electrons to peroxymonosulfate (PMS) [12]. $^1\text{O}_2$ is more inclined and selective for polycyclic aromatic hydrocarbon derivatives with electron-rich moieties ($-\text{NH}_2$ and $-\text{OH}$) [13]. During pollutant degradation process, various intermediates with different structure characteristics are generated. Therefore, we reasonably speculate that a more efficient and rapid pollutant removal performance can be possibly achieved via synergistically coupling of different non-radical regimes in one catalytic system. Although coexistence of different non-radical activation mechanisms on carbon [14–16] and MnOx catalysts [17,18] were previously reported, the pollutant removal rate by different reaction routes is not well-matched, leading to an unsatisfactory treatment performance. Appropriately designing two independent active sites on one catalyst and modulating their exposed numbers to achieve a reaction rate tradeoff between different non-radical pathways is then highly desired.

In this work, we aim to resolve the inferior mineralization issue of non-radical oxidation via synergizing ETP with $^1\text{O}_2$ in a PMS based heterogeneously catalytic oxidation system. To achieve this objective, N doping was employed as an effective tool to tune electronic structure of Mn based carbon catalyst and its catalytic activity was evaluated by quantitative analysis of PMS decomposition and diclofenac (DCF) degradation. Then, the reaction kinetics and contribution of $^1\text{O}_2$ and ETP to DCF degradation were identified and quantified. Also, the synergistic effect of two non-radical processes was validated via model degradation reaction, i.e., hypochlorous acid mediated $^1\text{O}_2$ evolution reaction and carbon nanotube (CNT) catalyzed ETP process. More importantly, we provide new insights into how the coupling mechanism of $^1\text{O}_2$ and ETP leads to the efficient and accelerated mineralization of DCF through theoretical calculation and quantitative structure-reactive activity relationship analysis. This work has a certain attraction for the sustainable degradation of organic pollutants in complex water matrices.

2. Materials and methods

2.1. Chemicals

Sodium alginate, calcium chloride anhydrous (CaCl_2), manganese chloride tetrahydrate ($\text{MnCl}_2 \cdot 4\text{H}_2\text{O}$), hydrochloric acid (HCl, 37%), sulfuric acid (H_2SO_4), urea ($\text{CH}_4\text{N}_2\text{O}$), diclofenac (DCF) 2,4,6-trichlorophenol (2,4,6-TCP), triclosan (TCS), bisphenol A (BPA), ciprofloxacin (CIP), 4-acetamidophenol (APAP), sulfamethazine (SM2), benzoic acid (BA), boric acid (H_3BO_3), sodium tetraborate decahydrate ($\text{Na}_2\text{B}_4\text{O}_7 \cdot 10\text{H}_2\text{O}$), PMS ($2\text{KHSO}_5 \cdot \text{KHSO}_4 \cdot \text{K}_2\text{SO}_4$, 47% KHSO_5 basis), carbon nanotube single-walled (95.0 wt%, outside diameter: 1–2 nm, length: 4–20 nm), methanol (MeOH), vitamin C, ethanol (EtOH), L-histidine, isopropyl alcohol (IPA), tert-butanol (TBA), β -carotene, acetonitrile, humic acid (HA) formic acid (CH_2O_2), phosphoric acid (H_3PO_4), 5,5-dimethyl-1-pyrroline-n-oxide (DMPO), 2,2,6,6-tetramethyl-4-piperidinol (TEMP), methyl phenyl sulfoxide (PMSO), hydrogen peroxide (H_2O_2 , 30.0%) sodium hypochlorite (NaClO), sodium ethoxide ($\text{C}_2\text{H}_5\text{ONa}$), 1,3-diphenylisobenzofuran (DPBF), N,N-dimethylformamide (DMF), acetonitrile, formic acid, potassium iodide (KI), sodium bicarbonate (NaHCO_3) were obtained from Sinopharm Chemical Reagent Co. Ltd. All chemicals used in this work were analytical grade without any purification.

2.2. Synthesis of catalysts

Mn based precursor was initially acquired via sol-gel method, as reported in our previous work [19]. In brief, 1 wt.% sodium alginate was dropwise added into 5 wt.% CaCl_2 solution under stirring to form gel

particle. Subsequently, 0.1 M Mn^{2+} were loaded into the hydrogel after dissociation of Ca^{2+} in 1 M HCl solution. The obtained Mn-loaded hydrogel was dried at 60°C and then used as the Mn-based precursors. In order to prepare metal carbon-based catalyst, 1.50 g of precursor was mixed with 0.30 g of urea and carbonized at 800°C for 2 h under N_2 atmosphere. Afterwards, the carbonated product was washed three times with 1 M HCl and rinsed with deionized water until the supernatant was neutral. Then, the precipitates were dehydrated in an oven at 60°C and denoted as Mn-C-N. Catalyst prepared with same procedure while without urea doping was denoted as Mn-C. In addition, in order to better elucidate the structure-activity relationship, the catalysts with different doping amount of Mn and N were respectively synthesized and their catalytic activities were evaluated. The doped Mn content was modulated by reducing the original 0.1 M Mn^{2+} to 0.01 M and 0.05 M while maintaining 0.3 g urea dosage during pyrolysis and the obtained catalysts were named 0.01 M Mn-C-N and 0.05 M Mn-C-N, respectively. Similarly, the doped N content was regulated via reducing urea dosage to 0.2 and 0.1 g and the obtained catalysts were named Mn-C-N_{0.2} g and Mn-C-N_{0.1} g.

To explore the potential influence of surface oxygen functional group on oxidative species formation, $\text{C}_2\text{H}_5\text{ONa}$ was selected as a typical ketone groups disruptor. To achieve this, 0.50 g of as-prepared catalyst was added to 100 mL of 0.05 M $\text{C}_2\text{H}_5\text{ONa}$ solution and stirred under light-proof conditions for 36 h. Then the obtained material was washed several times with pure water and dried in an oven at 70°C . The catalyst after $\text{C}_2\text{H}_5\text{ONa}$ solution treatment was named as Mn-C-N_{C=O}free and Mn-C-N_{C=O}free, respectively.

2.3. Pollutants degradation test

The catalytic performance of Mn-C-N was investigated by activating PMS to degrade DCF. In a typical degradation experiment, the as-prepared catalyst (0.2 g/L) was added into DCF solution (50 mg/L in borate buffer, $\text{pH} = 7$) and stirred for 20 min to ensure the adsorption-desorption equilibrium. Subsequently, 0.1 mL PMS stock solution was added to initiate the catalytic degradation reaction, at a final concentration of 0.6 mM. At certain time intervals, pipetting 0.5 mL of the reaction mixture into centrifuge tube that prefilled with 0.1 mL methanol, followed by immediate centrifugation at 13,000 rpm and then 200 μL of supernatant was withdrawn for the further analysis. To evaluate the reusability and stability of catalyst, catalyst after catalytic reaction was collected by filtration, rinsed and then vacuum dried at 60°C overnight for the next cycle of testing. Also, the degradation performance of other refractory pollutants including 2,4,6-TCP, TCS, BPA, CIP, APAP, and SM2 by catalytic oxidation system was evaluated.

2.4. Characterization and analytical methods

Instruments and methods used for characterizing catalyst structure are detailed in Text S1, including scanning electron microscope (SEM), transmission electron microscope (TEM), X-ray diffraction spectroscopy (XRD), organic elemental analysis, specific surface area analyzer (BET), Raman spectroscopy, and X-ray photoelectron spectroscopy (XPS).

Organic pollutant concentration was determined by high-performance liquid chromatography (LC-16, Shimadzu, Japan) and the specific instrument parameters are provided in Table S1. PMS content was detected by KI colorimetric method (Text S2). The intermediate products during DCF degradation were enriched via a C-18 column (water oasis HLB, Ireland) and analyzed by high-performance liquid chromatography-mass spectrometry (HPLC-MS/MS, Waters UPLC I-Class Xevo TQ-S micro, America). Electron paramagnetic resonance (EPR, Bruker A300 EPR Spectrometer, Germany) test allows the detection of reactive oxygen species generated during the degradation process [20]. DMPO was used to trap $\cdot\text{OH}$ and $\text{SO}_4^{\cdot-}$ and TEMP was used to capture $^1\text{O}_2$. Also, DPBF was used as a sensitive probe to semi-quantitative analysis of $^1\text{O}_2$ and the detailed procedure was provided in Text S3. A

constant-potential time-current response test was performed using an electrochemical workstation (CHI 760E, China) to identify the ETP mechanism. The specific experimental procedures are described in Text S4. The mineralization efficiency of the contaminants by oxidative system was detected by total organic carbon analyzer (TOC, TOC-L, Shimadzu, Japan).

2.5. Computational methods

All the calculations were conducted using Gaussian 16 [21] package. The geometry optimizations were performed with B3LYP [22,23]/Def2-TZVP [24,25] method with Grimme's empirical dispersion-correction (Grimme-D3BJ) [26,27]. Frequency analyses were conducted at the same level of theory to confirm the stationary points to be minimal. The HOMO/LUMO energies were calculated based on the optimized structures. The SMD [28] solvation model (considering water as the solvent) was introduced in all the calculations.

3. Results and discussion

3.1. Catalyst structure characteristics

Catalyst morphology and structure were initially characterized and analyzed. TEM and SEM images showed that Mn-C-N had a reticulated porous structure (Fig. 1a and b), which was different from the porous structure of Mn-C (Fig. S1a and b), probably due to the urea doping induced pore creation. BET and pore size analysis (Fig. S2a and b) further showed that N doping was beneficial for the formation of pores. The specific surface area of Mn-C-N was 1227 m²/g (Table S2), which facilitated the mass transfer diffusion of pollutants [29]. N 1s XPS spectrum (Fig. S3c) showed that Mn-C-N was rich in nitrogen-containing sites such as pyridinic N (398.3 eV), pyrrolic N (400.1 eV), and graphitic N (401.3 eV) [30]. Two carbon-related characteristic peaks of the catalysts located at 1340 cm⁻¹ (D-band) and 1590 cm⁻¹ (G-band) could be observed from Raman spectra (Fig. 1c), which can provide information about the disorder and crystallinity of the material [19]. The I_D/I_G value can reflect the degree of defects in carbon catalysts [31]. The calculated I_D/I_G values of 1.017 for Mn-C-N and 1.001 for Mn-C clearly indicated that the defect level of Mn-C-N was higher than that of Mn-C. XRD

spectra (Fig. 1d) showed a typical carbon-related peak from two materials. Organic elemental analysis (Table S3) illustrated that N was successfully doped into the catalyst. Since elemental Ca was added during catalyst preparation, the amount of Ca in the Mn-C-N was probed by ICP-OES. The results showed that Mn-C-N contained only 0.01 wt% of elemental Ca (Table S4). What's more, the EDS mapping image (Fig. 1e-h) further showed that Mn, N and C were uniformly distributed within the Mn-C-N. Based on these characterizations it was determined that Mn-C-N and Mn-C were successfully synthesized.

3.2. PMS activation performance of catalysts

PMS dissociation catalyzed by Mn-C-N and Mn-C was initially evaluated. As shown in Fig. 2a, Mn-C-N could catalytically decompose about 95% of PMS within 20 min. The apparent rate constant (k_{obs} , min⁻¹) of catalyzing PMS decomposition by Mn-C-N was 0.101 min⁻¹ (Fig. 2b), which was higher than that of Mn-C (0.051 min⁻¹), implying its superior catalytic activity [32]. When DCF was added to the PMS solution, the concentration of PMS did not change (Fig. S4), indicating that DCF had no effect on the dissociation of PMS. Afterwards, the pollutant removal performance of catalytic system was investigated by selecting DCF as a representative refractory pollutant. Since Mn-C-N owned a high specific surface area, its adsorption effect on DCF removal needs to be evaluated firstly. It was observed that 20 min pre-adsorption was adequate to achieve equilibrium and about 50% and 30% of DCF was removed via adsorption, for Mn-C-N and Mn-C, respectively (Fig. 2c). Degradation experiments (Fig. 2d) demonstrated that PMS alone was unable to oxidize DCF and the pH of the three reaction systems remained stable (Fig. S5). After reaction of 15 min, nearly all of DCF was degraded in Mn-C-N/PMS system. In comparison, the removal efficiency of Mn-C/PMS system was limited. The fitting result of degradation curve revealed that DCF removal followed *pseudo* first-order kinetics (Fig. 2e) and the reaction rate constants were calculated to be 0.26 min⁻¹ and 0.03 min⁻¹ for Mn-C-N/PMS and Mn-C/PMS, respectively. The normalized apparent rate constant (k_{SA} , g m⁻² min⁻¹) [33] of Mn-C-N was 6 folds higher than that of Mn-C (Fig. 2f). Furthermore, to verify whether the DCF was removed by degradation instead of adsorption on the catalyst surface, the catalyst after reaction was collected and immersed into ethanol for extracting the adsorbed pollutants [34,35]. As

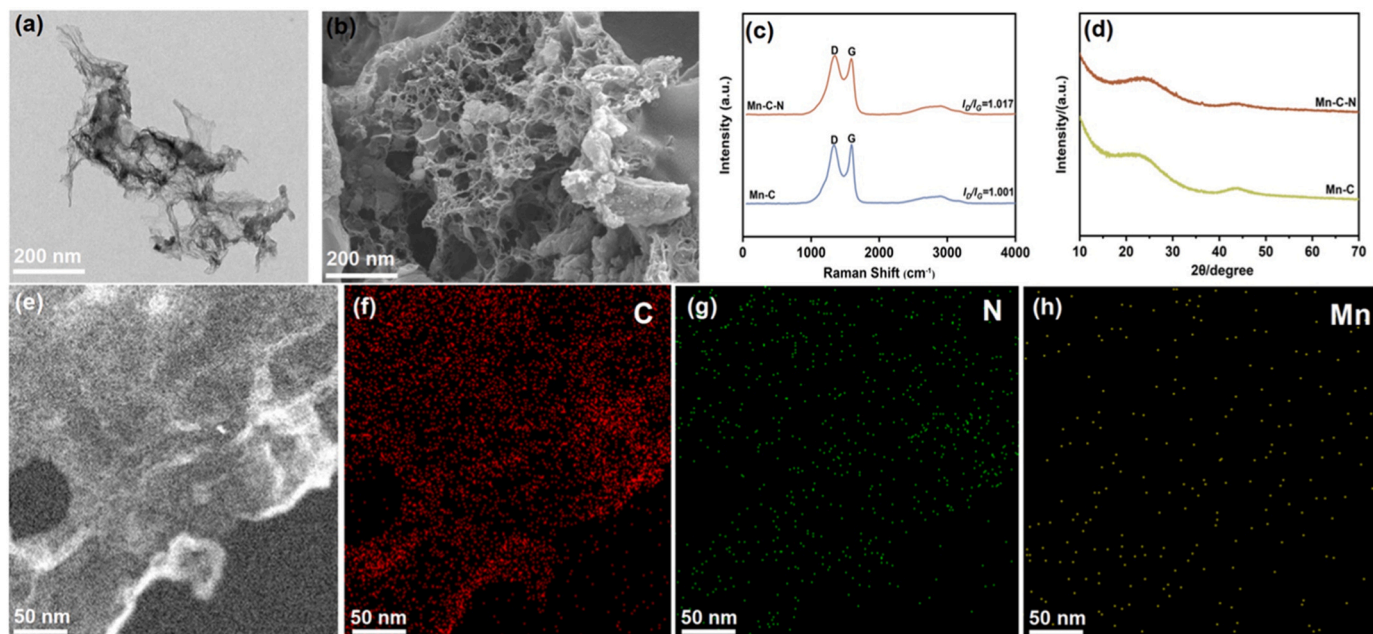


Fig. 1. Catalyst structure property characterization. (a) TEM and (b) SEM image of Mn-C-N. (c) Raman spectra of Mn-C-N and Mn-C. (d) XRD patterns of Mn-C-N and Mn-C. (e-h) The corresponding EDS mapping images of Mn-C-N.

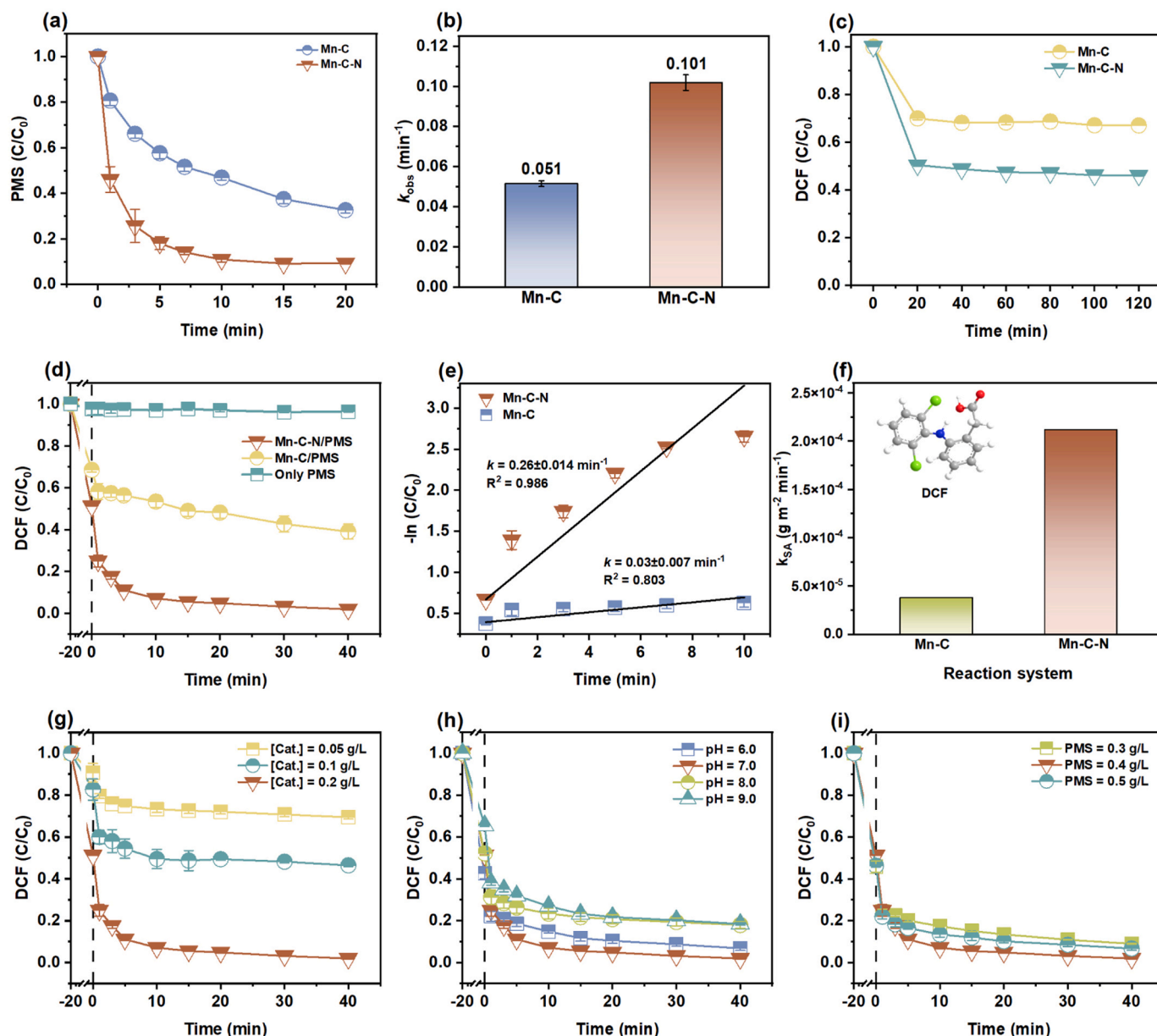


Fig. 2. Catalytic degradation performance evaluation. (a) PMS decomposition over the Mn-C-N and Mn-C and (b) the related decomposition rates. (c) Adsorption and (d) degradation curves of DCF by different reaction systems. (e) *Pseudo*-first-order kinetics of DCF degradation over catalysts via PMS activation. (f) Relationship between the specific activities (k_{SA}) of different catalysts. Effects of (g) catalyst dosages, (h) pH, and (i) PMS concentrations on the degradation of DCF. Reaction conditions: [catalysts] = 0.05 – 0.2 g/L, [DCF] = 50 mg/L, [PMS] = 0.3 – 0.5 g/L, pH = 6.0 – 9.0.

illustrated in Fig. S6a, when the PMS was not dosed, the extracted amount of DCF from Mn-C-N and Mn-C surface were 0.81 and 0.46 mg. However, after reaction with PMS, these values were 0.1 and 0.06 mg, which decreased by 87.7% and 87%, respectively. The TOC changes were also in agreement with the above results (Fig. S6b). Herein, the rapid and increased DCF removal in Mn-C-N/PMS system was due to degradation rather than adsorption.

Potential influences of several key parameters including catalyst dosage, PMS concentration, and pH on DCF degradation was further explored. It was observed that increasing catalyst dosage would result in a more rapid removal of DCF (Fig. 2g). This is mainly because increased catalyst amount would provide more active sites for PMS activation [36], which was then beneficial to improving pollutant removal. As shown in Fig. 2h and i, both the reaction pH and PMS dosage exhibited a limited influence on degradation of DCF by Mn-C-N. Therefore, the catalyst dosing amount of 0.2 g/L, PMS concentration of 0.4 g/L and pH

of 7 was selected as the optimal experimental conditions for the following mechanism study. Both the PMS activation and degradation experiments reflected that the catalytic performance of Mn-C-N was superior to that of Mn-C.

3.3. ETP and ¹O₂ identification and their generation mechanism elucidation

To identify the reactive species produced in the oxidation system, different quenchers were selected and added, where EtOH was used to both quench $\cdot\text{OH}$ ($k = 10^9 \text{ M}^{-1}\cdot\text{s}^{-1}$) and $\text{SO}_4^{\cdot-}$ ($k = 10^7 \text{ M}^{-1}\cdot\text{s}^{-1}$) [37] while TBA was for quenching $\cdot\text{OH}$ ($k = 3.8 \times 10^8 \sim 7.6 \times 10^8 \text{ M}^{-1}\cdot\text{s}^{-1}$) [38]. As shown in Fig. 3a and Fig. S7, alcohols exhibited a limited inhibition on degradation of DCF in two systems. EPR spectra illustrated that there were no signals when DMPO was added (Fig. S8). Furthermore, BA was selected as a chemical probe to explore the contribution of

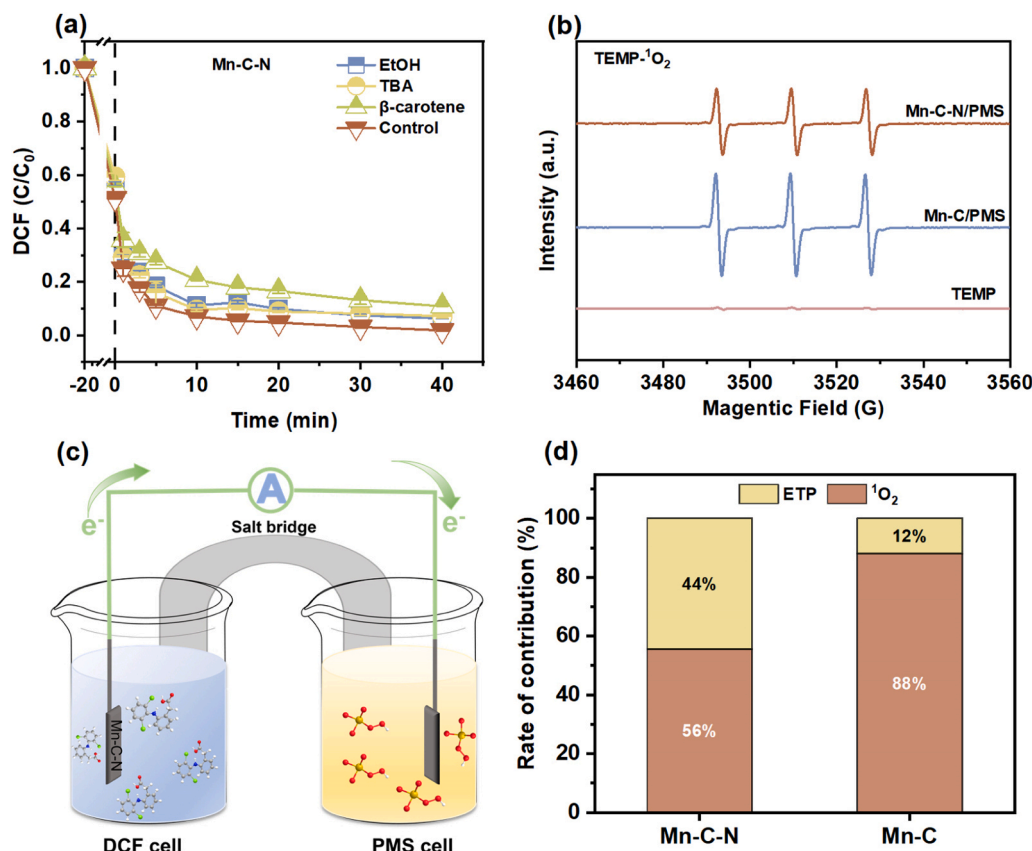


Fig. 3. Reactive oxidative species identification. (a) Effect of EtOH, TBA and β-carotene on DCF degradation in the Mn-C-N/PMS systems. (b) TEMP-trapped ¹O₂ spectra via EPR detection. (c) Schematic illustration of two-chamber galvanic oxidation reactor. (d) The contribution of ¹O₂ and ETP to DCF degradation in different catalytic systems. Reaction conditions: [catalysts] = 0.2 g/L, [DCF] = 50 mg/L, [PMS] = 0.4 g/L, pH = 7.0, [EtOH] = [TBA] = 130 mM, [β-carotene] = 0.37 mM, [DMPO] = [TEMP] = 60 mM.

radicals to DCF degradation, since BA has high reaction rates for SO₄^{•-} ($k = 1.2 \times 10^9 \text{ M}^{-1}\cdot\text{s}^{-1}$) and [•]OH ($k = 4.2 \times 10^9 \text{ M}^{-1}\cdot\text{s}^{-1}$) [12]. As shown in Fig. S9, DCF removal was not influenced by BA. Based on the above results, radicals were initially ruled out for DCF removal. Previous studies have documented that for metal based catalyst, high-valence metal intermediate might play an important role for pollutant removal [39–41]. Therefore, PMSO was used as a scavenger to investigate the potential formation of high-valence metal species during the degradation process [2]. As shown in Fig. S10, PMSO showed a negligible effect on the degradation of DCF in the Mn-C-N/PMS system, indicating that the high valence metal Mn is not generated. Herein, it was deduced that non-radical, i.e., ETP and ¹O₂, are the possible mechanism and responsible for DCF removal.

We next verified whether ¹O₂ was involved in the degradation of DCF. Although FFA ($k = 1.2 \times 10^8 \text{ M}^{-1}\cdot\text{s}^{-1}$) [12], L-histidine ($k = 3.2 \times 10^7 \text{ M}^{-1}\cdot\text{s}^{-1}$) [10], and NaN₃ ($k = 4.5 \times 10^8 \text{ M}^{-1}\cdot\text{s}^{-1}$) [42] are widely used as ¹O₂ quencher, they all directly reacted with PMS (Fig. S11), which may cause misjudgment. β-carotene is a kind of carotenoids, which appears a high reaction rate constant toward ¹O₂ ($k = 2.0 \sim 3.0 \times 10^{10} \text{ M}^{-1}\cdot\text{s}^{-1}$) [3] while with inert property to PMS (Fig. S11). The quenching experiment (Fig. 3a and Fig. S7) showed that the degradation rate of DCF was inhibited when β-carotene was added to the two systems. The quenching effect was different for the two systems, where Mn-C was completely inhibited while Mn-C-N was partially retarded. TEMP can be used to specifically capture ¹O₂, producing a TEMP-¹O₂ adduct with a 1:1:1 triplet state characteristic peak [43]. As shown in Fig. 3b, both of the Mn-C-N/PMS and Mn-C/PMS systems observed a typical 1:1:1 triplet peak signals from the EPR pattern, which further proved the existence of ¹O₂. It has been reported that DPBF can selectively react with ¹O₂ and thereby leading to its chromophore moiety

disappeared [44], which was useful to help judging whether ¹O₂ was generated. Compared to DPBF removal by adsorption (Fig. S12a and c), PMS addition would induce a significantly improved removal rate of this probe (Fig. S12d and d), further supporting the generation of ¹O₂ in Mn-C-N/PMS and Mn-C/PMS systems. Compared to the almost complete inhibition on DCF removal in Mn-C/PMS system, β-carotene addition only caused a partial inhibition in Mn-C-N/PMS. In order to further confirm the presence of ETP in the Mn-C-N/PMS system, we set up a galvanic oxidation reactor, so DCF can only be oxidized via ETP (Fig. 3c). After respectively adding DCF and PMS into separate two half-cells, a stable electric current with value of about $0.9 \times 10^{-4} \text{ A}$ could be observed. In addition, the constant potential time-to-current response test that had been widely adopted as an effective electrochemical method to demonstrate the presence of ETP [45] was also conducted. As shown in Fig. S13, the addition of PMS stimulated a significant increase in the current output, and then a change in the current density could be observed by adding DCF to the electrolyte for a certain period of time. Combining the above results, we concluded that DCF was removed via coupling effect of ¹O₂ and ETP in the Mn-C-N/PMS system.

Based on the *pseudo*-first-order kinetics ($-\ln(C/C_0) = kt$) (Fig. S14) of DCF oxidation in the presence of β-carotene quencher, the contributions of ¹O₂ and ETP to DCF oxidation in two different reaction systems were determined as follows:[46].

$$\lambda(^1\text{O}_2) = \frac{k_0 - k_1}{k_0} \times 100\% \quad (1)$$

$$\lambda(\text{ETP}) = 1 - \lambda(^1\text{O}_2) \quad (2)$$

where k_0 is the initial reaction rate constant without quenching agent,

and k_1 is the reaction rate constant after adding β -carotene. According to the above equations, the quantitative contribution of $^1\text{O}_2$ and ETP to DCF degradation was shown in Fig. 3d. It is worth noting that the Mn-C/PMS system was mainly a $^1\text{O}_2$ -dominated degradation process, whose contribution was up to 88%. When N was doped into Mn-C, a combination of $^1\text{O}_2$ and ETP were formed to accelerate the degradation of DCF. This indicates that the PMS activation pathway is closely related to the change of catalyst structure by N doping.

According to the Boehm titration principle [47], $\text{C}_2\text{H}_5\text{ONa}$ can destroy oxygen-containing functional groups. Herein, $\text{C}_2\text{H}_5\text{ONa}$ treatment was adopted to investigate whether oxygen-containing functional groups were involved in catalytic reaction. Results showed that (Fig. 4a and b), compared with the pristine catalyst, the degradation rate of DCF in the Mn-C- C=O_{free} /PMS system decreased, while the DCF removal in the Mn-C- $\text{N}_{\text{C=O}_{\text{free}}}$ /PMS system was negligibly affected. Therefore, we speculate that the oxygen-containing functional group structure in Mn-C may mediate the dissociation of PMS to produce $^1\text{O}_2$. Next, we carried out EPR experiments. It can be observed from the spectra that 1: 1: 1 characteristic peak appeared in the Mn-C- $\text{N}_{\text{C=O}_{\text{free}}}$ /PMS system, while there was no corresponding characteristic peak in the Mn-C- C=O_{free} /PMS system (Fig. 4c), indicating that no $^1\text{O}_2$ is generated in the Mn-C- C=O_{free} /PMS system. The DPBF probe detection also ruled out the possible generation of $^1\text{O}_2$ in the Mn-C- C=O_{free} /PMS system (Fig. S15a - b).

Therefore, for the Mn-C catalyst, the oxygen-containing functional group structure was responsible to catalyze PMS decomposition to produce $^1\text{O}_2$. While for Mn-C-N catalyst, the responsible catalytic sites were mainly from N doped structures. In Mn-C-N/PMS system, PMS dissociation may occur in the electron-deficient C atom near pyridinic N to generate $^1\text{O}_2$ [46]. When N was doped, Mn-N coordination structure

was formed, as evidenced from the characterization results of synchrotron radiation (Fig. 4d and Table S5), which increases the role of electron transfer in Mn-C-N. Therefore, in the Mn-C-N/PMS/DCF system, $^1\text{O}_2$ and ETP pathways were coupled, and the degradation efficiency of DCF was significantly improved.

To get in-depth into the activity-structure relationship, the Mn-C-N catalysts with different amounts of Mn and N doping, i.e. 0.01 M Mn-C-N, 0.05 M Mn-C-N, Mn-C- $\text{N}_{0.2\text{g}}$ and Mn-C- $\text{N}_{0.1\text{g}}$ were fabricated and their catalytic performances were evaluated. As shown in Fig. 5a, all four as-prepared catalysts could activate PMS and result in DCF degradation (Fig. 5b and c). Subsequently, quenching experiments (Fig. 5d and Fig. S16), EPR spectra (Fig. 5e), and the constant potential time-to-current response curves (Fig. 5f) demonstrated the existence of both $^1\text{O}_2$ and ETP for all four oxidation systems. Moreover, the contributions of $^1\text{O}_2$ and ETP to the removal of DCF are shown in Fig. 5g. Since ETP is regulated by the Mn-N site, its contribution gradually increases with increasing Mn content. However, the decrease in N content reduced the contribution of $^1\text{O}_2$ to the removed DCF from 73% to 38%.

3.4. Synergetic mechanism between ETP and $^1\text{O}_2$ on Mn-C-N

To verify that the $^1\text{O}_2$ can synergize with ETP in the Mn-C-N/PMS system to achieve a "1 + 1 > 2" effect, model reactions including $^1\text{O}_2$ evolution via chemical reaction of H_2O_2 and OCl^- [48–50] and ETP driven by CNT/PMS were respectively conducted and their contribution to DCF removal was evaluated. Quenching results clearly showed that these two systems were respectively ETP and $^1\text{O}_2$ dominated (Fig. S18). In order to ensure that the steady-state concentration of the $^1\text{O}_2$ produced by the $\text{H}_2\text{O}_2 + \text{NaClO}$ system and the electron flux produced by the CNT/PMS system were the same as that of the Mn-C-N/PMS system,

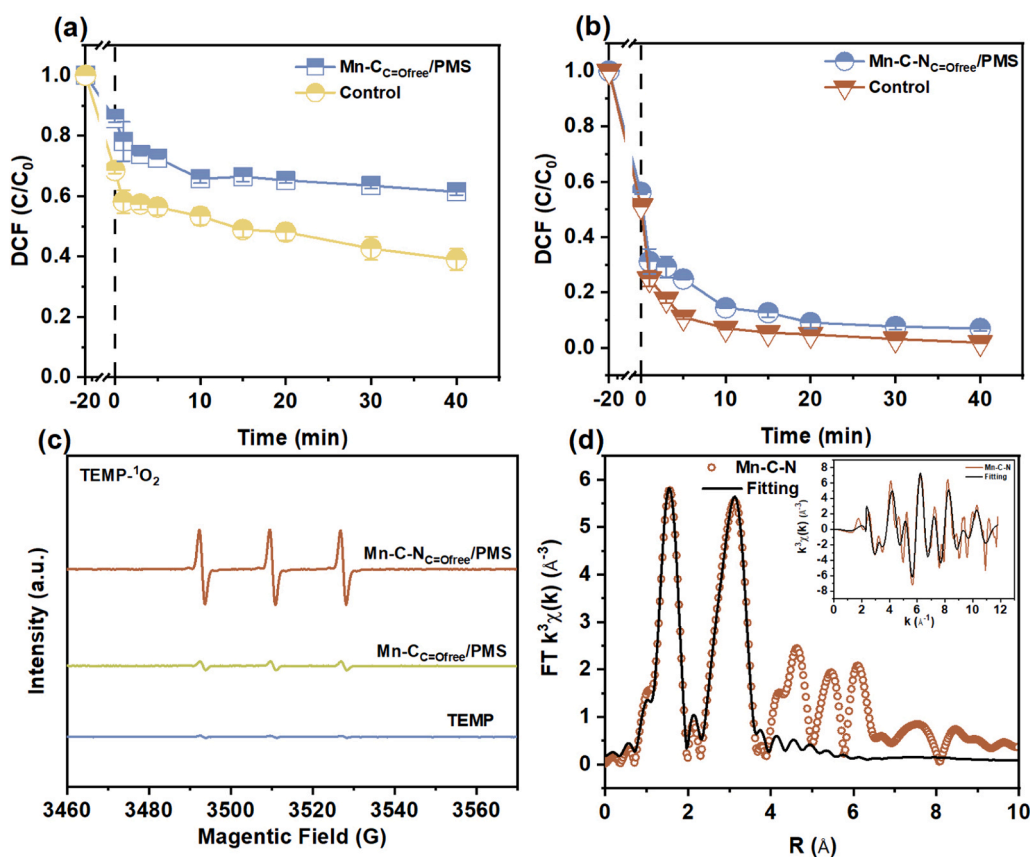


Fig. 4. Catalytic active site exploration. DCF degradation curves by (a) Mn-C- C=O_{free} /PMS system and (b) Mn-C- $\text{N}_{\text{C=O}_{\text{free}}}$ /PMS system. (c) TEMP-trapped $^1\text{O}_2$ spectra via EPR detection. (d) Fourier-transformed EXAFS spectra of Mn-C-N (the inserted figure is the K space fitting curve). Reaction conditions: [DCF] = 50 mg/L, [catalysts] = 0.2 g/L, [PMS] = 0.4 g/L, pH = 7.0, [TEMP] = 60 mM.

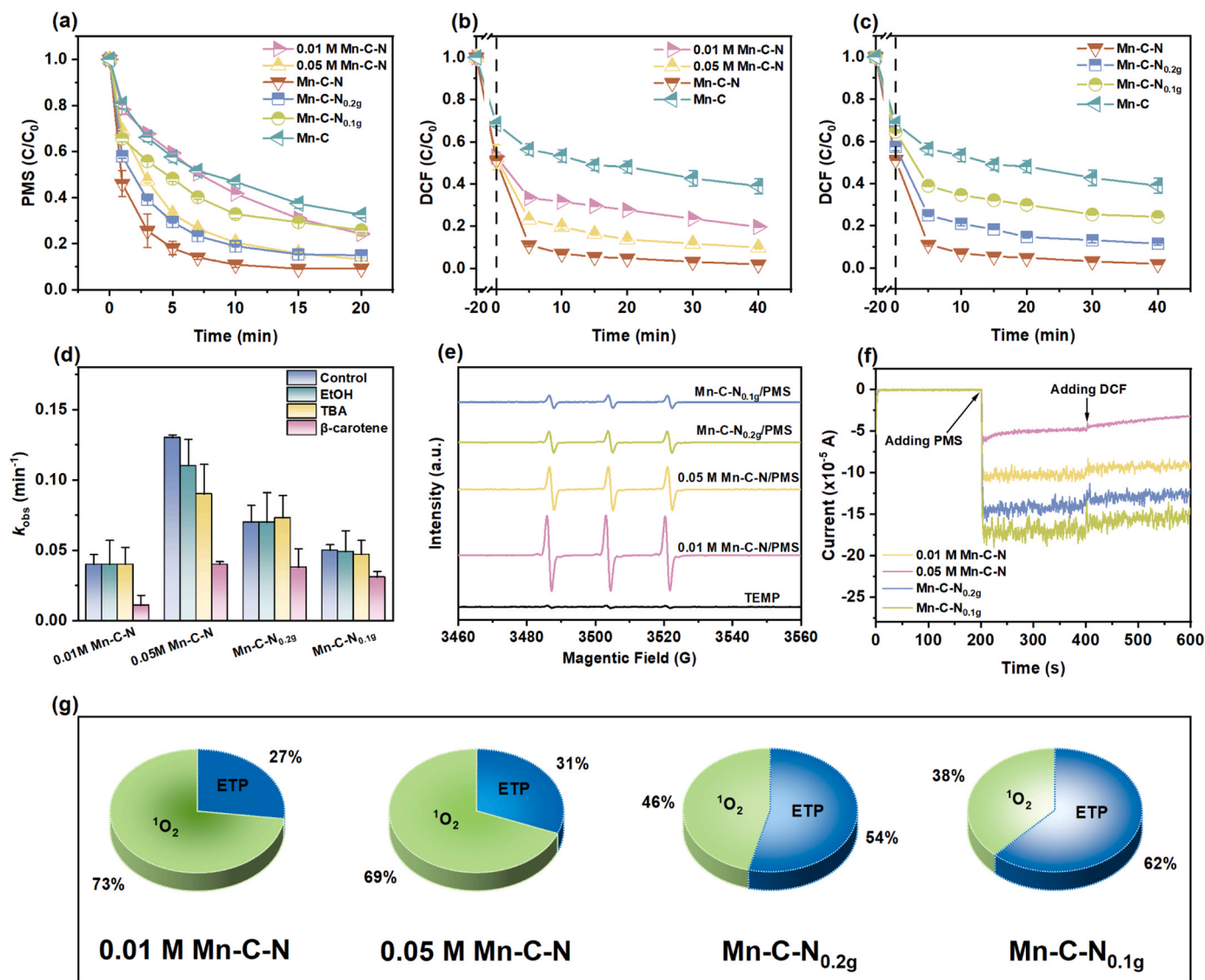


Fig. 5. Regulation of $^1\text{O}_2$ and ETP contributions to DCF removal. (a) PMS decomposition over the different catalysts. (b) and (c) The degradation curves of DCF by different reaction systems. (d) The k_{obs} of DCF degradation by dosing different quenchers into oxidation system. (e) EPR spectra in different catalysts/PMS systems with TEMP as the trapping agent. (f) Amperometric i - t curve. (g) The contribution of $^1\text{O}_2$ and ETP to DCF degradation in different catalytic systems. Reaction conditions: [catalysts] = 0.2 g/L, [DCF] = 50 mg/L, [PMS] = 0.4 g/L, pH = 7.0, [EtOH] = [TBA] = 130 mM, [β -carotene] = 0.37 mM, [DMPO] = [TEMP] = 60 mM.

quenching experiments (Text S5) and electrochemical experiments (Text S6) were performed, respectively. When the concentrations of H_2O_2 and NaClO were 0.5 mM, the steady-state concentrations of $^1\text{O}_2$ were calculated to be similar to the Mn-C-N/PMS system (Fig. S19). Also, for CNT/PMS system, the dosed CNT amount was adjusted to ensure that the total electron transfer amount (Q) was the same with that of Mn-C-N/PMS system (Fig. S20). On this basis, the degradation and mineralization rate of DCF were compared for different systems.

As shown in Fig. 6 and S21, the degradation rate as well as the reaction rate constants of the Mn-C-N/PMS system for DCF were higher than those of other oxidation systems. In addition, the mineralization performance was evaluated by measuring the TOC value of the solution before and after the catalytic reaction. As shown in Fig. 6c, the TOC removal efficiency by Mn-C-N/PMS system was as high as 80% within 1 h, proving the good mineralization ability of the system. Although ETP (CNT/PMS system) was able to degrade DCF (Fig. 6a), this process was incapable to mineralize pollutant, as evidenced by the unchanged TOC value along with the 5 h reaction time (Fig. 6c). In comparison, H_2O_2 + NaClO homogeneous system only mineralized about 40% of DCF. As a

result, a synergetic effect between the $^1\text{O}_2$ and ETP must be existed in the Mn-C-N/PMS system, further accelerating the removal and mineralization rate of DCF.

After analyzing the total ion chromatograms and referring to the degradation pathways of DCF by different methods reported in the literatures [51–55], the DCF degradation intermediates and their structures were obtained, as show in Table S6 and Fig. S22. The degradation pathways of DCF by the Mn-C-N/PMS system can be divided into three types (Fig. 6d). In pathway I, DCF may be dechlorinated to form P1 and P2, followed by hydroxylation and C-N breakage to form P3 and P4. In pathway II, $^1\text{O}_2$ and ETP alternatively attacked organic molecules to form P5, P6, P7, P8, P9 and P10 intermediates through hydroxylation, oxidation, dechlorination and C-N breakage. In pathway III, the -COOH group on DCF was decarboxylated to form the product P11. After that, P12, P13, and P14 were formed via formylation, hydroxylation, and C-N bond breaking, respectively. To further investigate the relation between compound structures and their reactivity, density function theory calculation was performed to calculate the highest occupied molecular orbital (E_{HOMO}) and the lowest unoccupied molecular orbital (E_{LUMO})

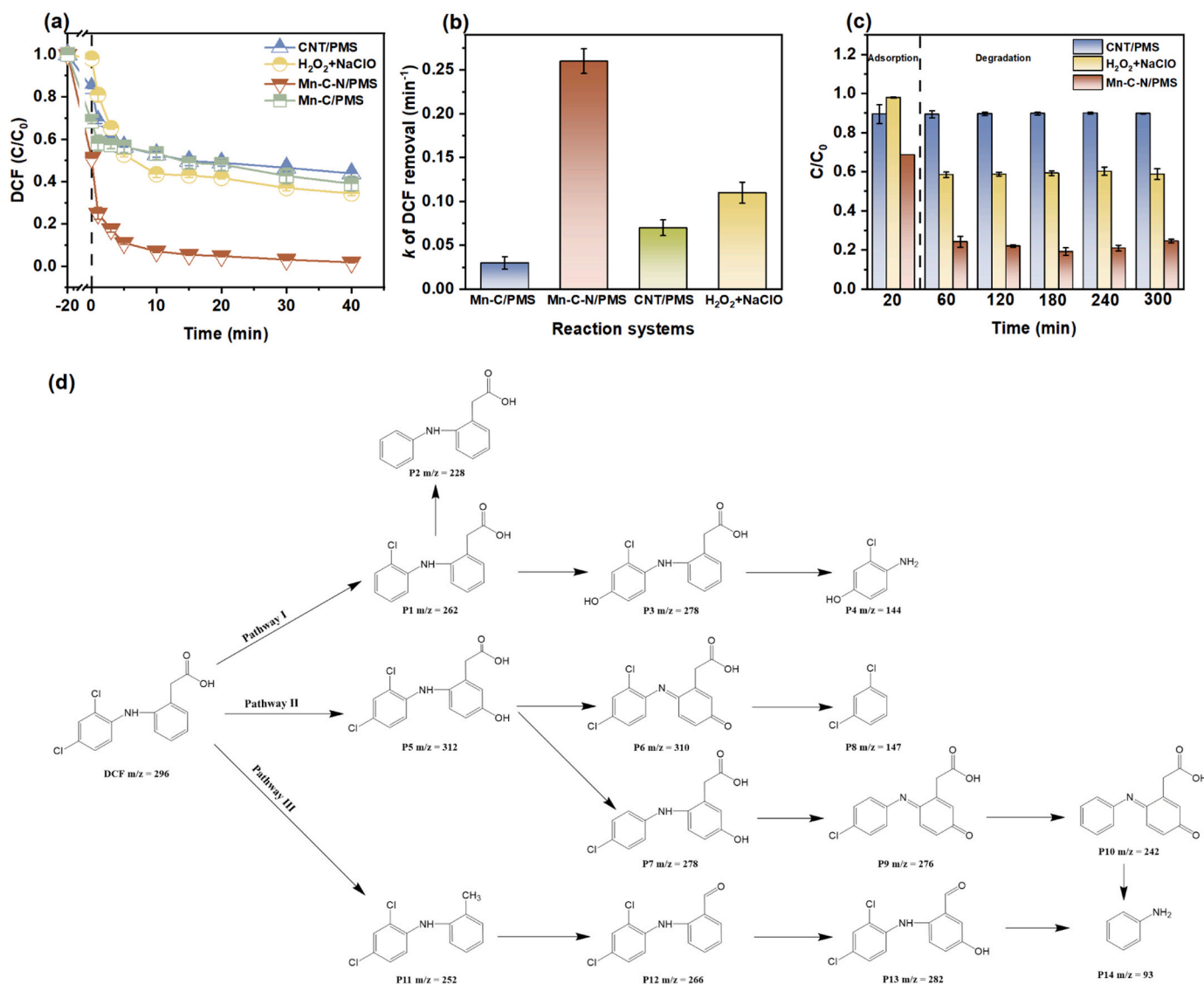


Fig. 6. DCF degradation by the ETP and $^1\text{O}_2$ analogous systems. (a) The degradation curve and (b) *Pseudo*-first-order kinetics of DCF in different reaction systems. (c) Change of TOC content in different reaction systems. (d) Proposed pathways of DCF degradation in Mn-C-N/PMS system. Reaction conditions: [catalysts] = 0.2 g/L, [CNT] = 0.1 g/L, [H₂O₂] = [NaClO] = 0.5 mM, [DCF] = 50 mg/L, [PMS] = 0.4 g/L, pH = 7.0.

energies. Among molecules, the electrons on E_{HOMO} are the most energetic and the least bound, and therefore the most reactive, susceptible to losing electrons and being attacked by $^1\text{O}_2$ [56,57], and conversely, E_{LUMO} has the lowest energy of all the unoccupied orbitals and is the most susceptible to accepting electrons. The narrowing of the energy gap (ΔE) between E_{HOMO} and E_{LUMO} implies that the ETP dominates the oxidizing system, resulting in effective removal of pollutants [58,59]. The E_{HOMO} and E_{LUMO} levels of several intermediates were calculated (Table S7). It could be known that DCF and most of its derivative were with a high E_{HOMO} , which matched well with the E_{LUMO} of $^1\text{O}_2$, suggesting their potential high reactivity with $^1\text{O}_2$. In comparison, the E_{LUMO} of intermediates P10 and P12 were lower than the other molecules and the ΔE ($E_{\text{LUMO}} - E_{\text{HOMO}}$) of P10 and P12 was 3.07 and 3.75 eV, respectively. Such a low E_{LUMO} and ΔE value of P10 and P12 indicates that these two compounds were more likely to undergo electrophilic attack via ETP at the electron-rich region. In conclusion, DCF degradation occurred with C-N bond breaking, decarboxylation, dehydrogenation, formylation, oxidation reactions [53,55,60–63], and finally were mineralized to CO₂ and H₂O. The degradation intermediates derived from the $^1\text{O}_2$ oxidation was possibly to be rapidly transformed via ETP and the alternative reactions of DCF and its derivative with $^1\text{O}_2$ and ETP

finally resulted in an improved mineralization performance.

3.5. Application potential of non-radical oxidation system

Recycling tests were conducted to assess the stability and reusability of Mn-C-N for the PMS-based degradation system. As shown in Fig. 7a, the catalytic degradation efficiency of this system remained at 80% after 5 cycles of reaction, indicating that the system can stably remove DCF. Considering that the wastewater is rich in inorganic anions and natural organic matter, the influences of some inorganic anions (e. g. Cl⁻, HCO₃⁻, H₂PO₄⁻) and humic acid on the degradation of DCF by Mn-C-N catalyzed PMS were evaluated (Fig. 7b). It can be seen that these composite substrates had no adverse effect on DCF degradation, indicating that Mn-C-N can be stably worked under a practical scenario [46]. Consistently, XRD pattern (Fig. 7c) of Mn-C-N catalyst before and after degradation experiment showed negligible change. Besides the DCF, the Mn-C-N/PMS system was also effective in removing other refractory organic pollutants such as 2,4,6-TCP, TCS, BPA, CIP, APAP and SM2 (Fig. 7d). The fitting results of the degradation curves showed that the reaction rate constants of the six pollutants tend to be similar (Fig. 7e and Fig. S23), indicating its universality.

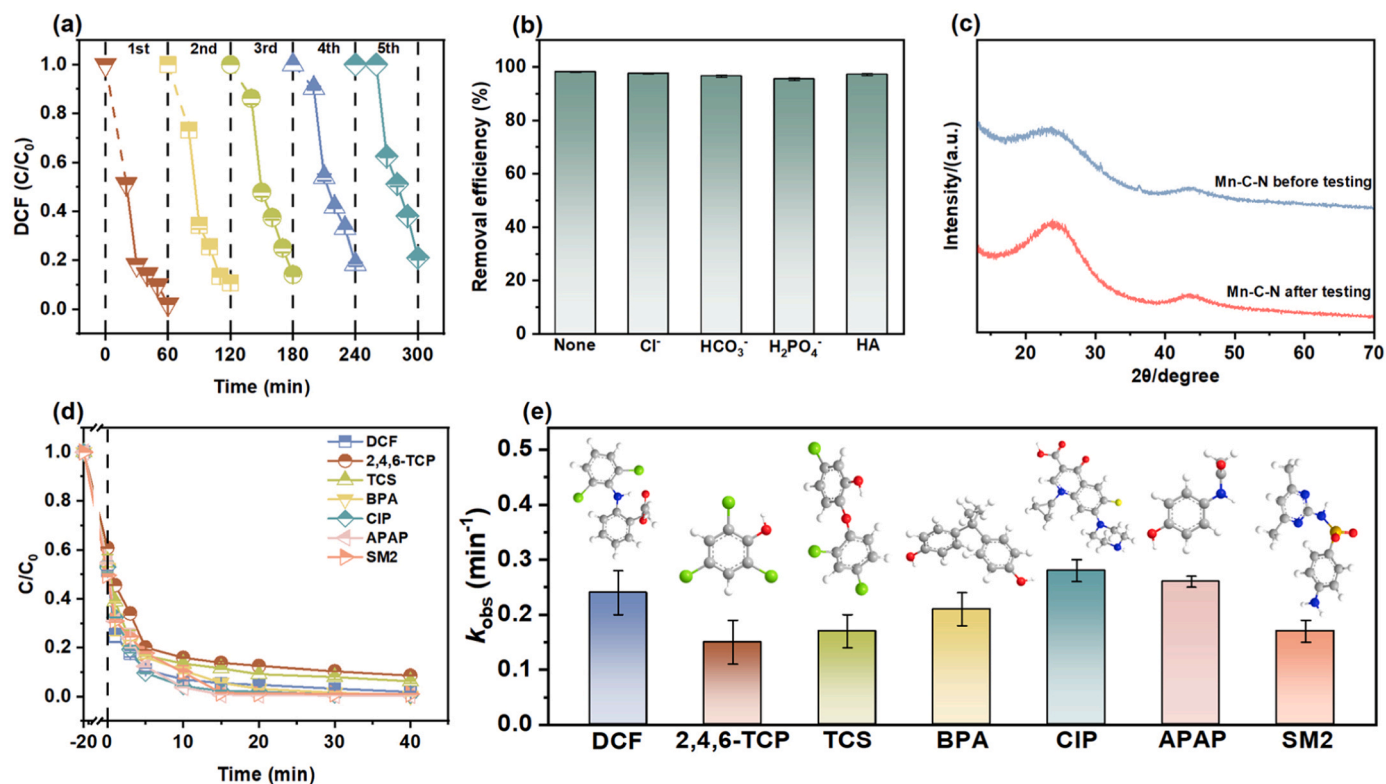


Fig. 7. The stability and universality of Mn-C-N. (a) Stability tests of Mn-C-N. (b) Interference by background dissolved solutes. (c) XRD patterns of Mn-C-N before and after reaction. (d) Feasibility of removing other refractory organic pollutants by Mn-C-N/PMS system and (e) the related degradation rates. Reaction conditions: [Mn-C-N] = 0.2 g/L, [DCF] = [2,4,6-TCP] = [TCS] = [BPA] = [CIP] = [APAP] = [SM2] = 50 mg/L, pH = 7.0, [PMS] = 0.4 g/L, [Cl⁻] = [HCO₃⁻] = [H₂PO₄⁻] = 2 mM, [HA] = 2 mg/L.

Further, in order to explore the application potential of Mn-C-N catalyst in treating actual wastewater, the local Yuhangtang River and tap water were collected and the DCF degradation performance were evaluated. From Fig. 8a, it can be seen that the Mn-C-N/PMS system worked well and nearly 100% of DCF was degraded within 15 min. Also, the TOC results (Fig. 8b) showed that the Mn-C-N/PMS system can mineralize 70% of the DCF into H₂O and CO₂ within 1 h, which proves the good mineralization ability of the system. Moreover, the treatment performance of livestock wastewater and secondary effluent by Mn-C-N/PMS was explored. It was found that the total chemical oxygen demand of livestock wastewater reduced by 70% and the color changed from yellow to clear, after treating by oxidation system for 40 min (Fig. 8c). In addition, the Mn-C-N/PMS system exhibited a good TOC mineralization performance for both wastewaters (Fig. 8d). Overall, the Mn-C-N catalyst has a good stability and practical application potential.

Selective oxidation of organic pollutant via non-radical is a promising wastewater treatment technology that can greatly reduce the overall chemical usage and operation costs accordingly. Although non-radicals remain active under complex background water constitutes, their weak oxidation ability stands as a big challenge for its practical application [64]. In this work, the above issue was well addressed by retrofitting a heterogeneous oxidation system where ETP and ¹O₂ were spontaneously generated. By taking N doping strategy and suitably exposing independent active sites amounts within Mn-C-N catalyst, the contribution of ETP and ¹O₂ to DCF degradation can be well modulated. The above synergistic effect between ¹O₂ and ETP may provide guidance for a novel non-radical oxidation system design and moving this technology forward practical application. Our work also directly demonstrates the feasibility of catalytic oxidation of wastewater with a low-carbon emission in the future, i.e., from a broader life cycle perspective, reducing chemical dependence means a reduced total carbon emission.

4. Conclusions

In this work, the unsatisfied pollutants mineralization issue of non-radical oxidation technology was resolved by retrofitting a heterogeneous oxidation system where ETP and ¹O₂ were spontaneously generated. By taking N doping strategy and thereby modulating the electronic structure of Mn-C-N catalyst, the contribution of PMS-associated ETP and ¹O₂ to DCF degradation was well matched. The normalized apparent rate constant obtained from the Mn-C-N was 6 folds higher than that of Mn-C. Mechanism interpretation revealed that the DCF intermediates derived from ¹O₂ oxidation could be rapidly transformed via ETP and thereby speeding up the overall mineralization rate. Repeated experiments and various pollutant degradation experiments showed that the catalytic system had long-term stability. Also, under 0.2 g/L Mn-C-N, 50 mg/L diclofenac, 0.4 g/L PMS, and actual water quality conditions, Mn-C-N/PMS system can efficiently mineralize 70% of DCF within 1 h. The results of this work might provide guidance for designing and applying a more efficient and chemical-saving non-radical oxidation system.

CRediT authorship contribution statement

Yun-Xin Huang: Conceptualization, Methodology, Software, Visualization, Writing – original draft. **Ke-Yu Chen:** Formal analysis. **Shi-Xu Wang:** Investigation, Validation. **Shou-Yan Zhao:** Investigation, Formal analysis. **Lin-Qian Yu:** Investigation, Validation. **Bao-Cheng Huang:** Conceptualization, Funding acquisition, Writing – review & editing. **Ren-Cun Jin:** Writing – review & editing, Supervision.

Declaration of Competing Interest

The authors declare that they have no known competing financial

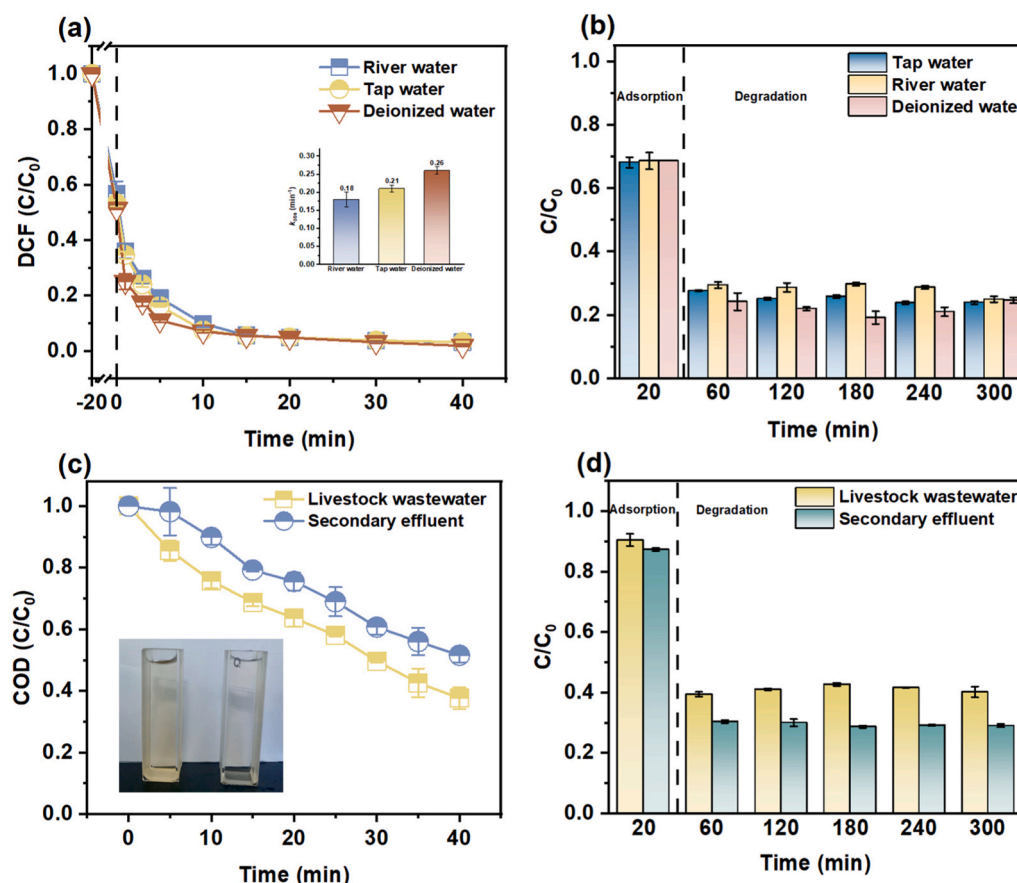


Fig. 8. Practical application potential of the non-radical oxidation system. (a) DCF degradation curve (the inset figure is *Pseudo*-first-order kinetics) and (b) TOC changes in different water bodies. (c) The COD (the inset figure is the color change of livestock wastewater before and after reaction) and (d) TOC changes of different wastewaters after treating by Mn-C-N/PMS system. Reaction conditions: [Mn-C-N] = 0.2 g/L, [DCF] = 50 mg/L, pH = 7.0, [PMS] = 0.4 g/L.

interests or personal relationships that could have appeared to influence the work reported in this paper.

Data availability

Data will be made available on request.

Acknowledgments

The authors wish to thank the National Natural Science Foundation of China (51908172) and “Pioneer” and “Leading Goose” R&D Program of Zhejiang (2023C03149) for the financial support of this work.

Appendix A. Supporting information

Supplementary data associated with this article can be found in the online version at [doi:10.1016/j.apcatb.2023.123324](https://doi.org/10.1016/j.apcatb.2023.123324).

References

- W. Zhao, Z. Duan, Z. Zheng, B. Li, Cobalt bismuth oxide with cobalt (II/III) as a new stable peroxymonosulfate activator for effective degradation, mineralization, and detoxification of diclofenac in water, *J. Clean. Prod.* 365 (2022), 132781.
- Y. Wei, J. Miao, J. Ge, J. Lang, C. Yu, L. Zhang, P.J.J. Alvarez, M. Long, Ultrahigh peroxymonosulfate utilization efficiency over CuO nanosheets via heterogeneous Cu (III) formation and preferential electron transfer during degradation of phenols, *Environ. Sci. Technol.* 56 (2022) 8984–8992.
- X. Wang, Z. Xiong, H. Shi, Z. Wu, B. Huang, H. Zhang, P. Zhou, Z. Pan, W. Liu, B. Lai, Switching the reaction mechanisms and pollutant degradation routes through active center size-dependent Fenton-like catalysis, *Appl. Catal. B Environ.* 329 (2023), 122569.
- A. Tufail, W.E. Price, F.I. Hai, A critical review on advanced oxidation processes for the removal of trace organic contaminants: a voyage from individual to integrated processes, *Chemosphere* 260 (2020), 127460.
- Y. Feng, H. Li, L. Lin, L. Kong, X. Li, D. Wu, H. Zhao, K. Shih, Degradation of 1,4-dioxane via controlled generation of radicals by pyrite-activated oxidants: synergistic effects, role of disulfides, and activation sites, *Chem. Eng. J.* 336 (2018) 416–426.
- W. Ren, L. Xiong, G. Nie, H. Zhang, X. Duan, S. Wang, Insights into the electron-transfer regime of peroxydisulfate activation on carbon nanotubes: the role of oxygen functional groups, *Environ. Sci. Technol.* 54 (2020) 1267–1275.
- L. Zhang, X. Jiang, Z. Zhong, L. Tian, Q. Sun, Y. Cui, X. Lu, J. Zou, S. Luo, Carbon nitride supported high-loading Fe single-atom catalyst for activation of peroxymonosulfate to generate ¹O₂ with 100% selectivity, *Angew. Chem. Int. Ed.* 60 (2021) 21751–21755.
- H. Li, C. Shan, B. Pan, Fe (III)-doped g-C₃N₄ mediated peroxymonosulfate activation for selective degradation of phenolic compounds via high-valent iron-oxo species, *Environ. Sci. Technol.* 52 (2018) 2197–2205.
- X. Duan, H. Sun, Y. Wang, J. Kang, S. Wang, N-doping-induced nonradical reaction on single-walled carbon nanotubes for catalytic phenol oxidation, *ACS Catal.* 5 (2015) 553–559.
- C. Zhao, L. Meng, H. Chu, J.-F. Wang, T. Wang, Y. Ma, C.-C. Wang, Ultrafast degradation of emerging organic pollutants via activation of peroxymonosulfate over Fe₃C/Fe@N-C-x: singlet oxygen evolution and electron-transfer mechanisms, *Appl. Catal. B Environ.* 321 (2023), 122034.
- P. Yang, Y. Long, W. Huang, D. Liu, Single-atom copper embedded in two-dimensional MXene toward peroxymonosulfate activation to generate singlet oxygen with nearly 100% selectivity for enhanced Fenton-like reactions, *Appl. Catal. B Environ.* 324 (2023), 122245.
- R. Huang, P. Gao, J. Zhu, Y. Zhang, Y. Chen, S. Huang, G. Wang, Z. Yu, S. Zhao, S. Zhou, Insights into the pollutant electron property inducing the transformation of peroxymonosulfate activation mechanisms on manganese dioxide, *Appl. Catal. B Environ.* 317 (2022), 121753.
- M. Yang, Z. Hou, X. Zhang, B. Gao, Y. Li, Y. Shang, Q. Yue, X. Duan, X. Xu, Unveiling the origins of selective oxidation in single-atom catalysis via Co-N₄-C intensified radical and nonradical pathways, *Environ. Sci. Technol.* 56 (2022) 11635–11645.

- [14] E.-T. Yun, J.H. Lee, J. Kim, H.-D. Park, J. Lee, Identifying the nonradical mechanism in the peroxymonosulfate activation process: singlet oxygenation versus mediated electron transfer, *Environ. Sci. Technol.* 52 (2018) 7032–7042.
- [15] S. Adil, W.S. Kim, T.H. Kim, S. Lee, S.W. Hong, E.-J. Kim, Defective, oxygen-functionalized multi-walled carbon nanotubes as an efficient peroxymonosulfate activator for degradation of organic pollutants, *J. Hazard. Mater.* 396 (2020), 122757.
- [16] X. Duan, H. Sun, S. Wang, Metal-free carbocatalysis in advanced oxidation reactions, *Acc. Chem. Res.* 51 (2018) 678–687.
- [17] N. Tian, X. Tian, Y. Nie, C. Yang, Z. Zhou, Y. Li, Biogenic manganese oxide: an efficient peroxymonosulfate activation catalyst for tetracycline and phenol degradation in water, *Chem. Eng. J.* 352 (2018) 469–476.
- [18] L. Wang, J. Jiang, S.-Y. Pang, Y. Zhou, J. Li, S. Sun, Y. Gao, C. Jiang, Oxidation of bisphenol A by nonradical activation of peroxymonosulfate in the presence of amorphous manganese dioxide, *Chem. Eng. J.* 352 (2018) 1004–1013.
- [19] L.-Q. Yu, W.-J. Xiao, W.-J. Ma, T.-E. Wen, S.-L. Chen, F. Jin, B.-C. Huang, R.-C. Jin, Universal method to fabricate transition metal single-atom-anchored carbon with excellent oxygen reduction reaction activity, *ACS Appl. Mater. Interfaces* 13 (2021) 13534–13540.
- [20] M.J. Davies, Detection and characterisation of radicals using electron paramagnetic resonance (EPR) spin trapping and related methods, *Methods* 109 (2016) 21–30.
- [21] M.J. Frisch, G.W. Trucks, H.B. Schlegel, G.E. Scuseria, M.A. Robb, J.R. Cheeseman, G. Scalmani, V. Barone, G.A. Petersson, H. Nakatsuji, X. Li, M. Caricato, A.V. Marenich, J. Bloino, B.G. Janesko, R. Gomperts, B. Mennucci, H.P. Hratchian, J.V. Ortiz, A.F. Izmaylov, J.L. Sonnenberg, Williams, F. Ding, F. Lipparini, F. Egidi, J. Goings, B. Peng, A. Petrone, T. Henderson, D. Ranasinghe, V.G. Zakrzewski, J. Gao, N. Rega, G. Zheng, W. Liang, M. Hada, M. Ehara, K. Toyota, R. Fukuda, J. Hasegawa, M. Ishida, T. Nakajima, Y. Honda, O. Kitao, H. Nakai, T. Vreven, K. Throssell, J.A. Montgomery Jr., J.E. Peralta, F. Ogliaro, M.J. Bearpark, J.J. Heyd, E.N. Brothers, K.N. Kudin, V.N. Staroverov, T.A. Keith, R. Kobayashi, J. Normand, K. Raghavachari, A.P. Rendell, J.C. Burant, S.S. Iyengar, J. Tomasi, M. Cossi, J.M. Millam, M. Klene, C. Adamo, R. Cammi, J.W. Ochterski, R.L. Martin, K. Morokuma, O. Farkas, J.B. Foresman, D.J. Fox, *Gaussian 16 Rev. C.01*, (2016).
- [22] A.D. Becke, Density-functional exchange-energy approximation with correct asymptotic behavior, *Phys. Rev. A* 38 (1988) 3098–3100.
- [23] C. Lee, W. Yang, R.G. Parr, Development of the colle-salvetti correlation-energy formula into a functional of the electron density, *Phys. Rev. B* 37 (1988) 785–789.
- [24] F. Weigend, Accurate coulomb-fitting basis sets for H to Rn, *Phys. Chem. Chem. Phys.* 8 (2006) 1057–1065.
- [25] F. Weigend, R. Ahlrichs, Balanced basis sets of split valence, triple zeta valence and quadruple zeta valence quality for H to Rn: design and assessment of accuracy, *Phys. Chem. Chem. Phys.* 7 (2005) 3297–3305.
- [26] S. Grimme, J. Antony, S. Ehrlich, H. Krieg, A consistent and accurate ab initio parametrization of density functional dispersion correction (DFT-D) for the 94 elements H-Pu, *J. Chem. Phys.* 132 (2010), 154104.
- [27] S. Grimme, S. Ehrlich, L. Goerigk, Effect of the damping function in dispersion corrected density functional theory, *J. Comput. Chem.* 32 (2011) 1456–1465.
- [28] A.V. Marenich, C.J. Cramer, D.G. Truhlar, Universal solvation model based on solute electron density and on a continuum model of the solvent defined by the bulk dielectric constant and atomic surface tensions, *J. Phys. Chem. B* 113 (2009) 6378–6396.
- [29] L. Xu, B. Fu, Y. Sun, P. Jin, X. Bai, X. Jin, X. Shi, Y. Wang, S. Nie, Degradation of organic pollutants by Fe/N co-doped biochar via peroxymonosulfate activation: synthesis, performance, mechanism and its potential for practical application, *Chem. Eng. J.* 400 (2020), 125870.
- [30] Z. Guo, Y. Xie, J. Xiao, Z.-J. Zhao, Y. Wang, Z. Xu, Y. Zhang, L. Yin, H. Cao, J. Gong, Single-atom Mn–N₄ site-catalyzed peroxone reaction for the efficient production of hydroxyl radicals in an acidic solution, *J. Am. Chem. Soc.* 141 (2019) 12005–12010.
- [31] K. Zhang, P. Sun, M.C.A.S. Faye, Y. Zhang, Characterization of biochar derived from rice husks and its potential in chlorobenzene degradation, *Carbon* 130 (2018) 730–740.
- [32] Y. Wei, J. Miao, P.J.J. Alvarez, M. Long, How to accurately assess the intrinsic activity of catalysts in peroxo activation, *Environ. Sci. Technol.* 56 (2022) 10557–10559.
- [33] J. Miao, Y. Zhu, J. Lang, J. Zhang, S. Cheng, B. Zhou, L. Zhang, P.J.J. Alvarez, M. Long, Spin-state-dependent peroxymonosulfate activation of single-atom M–N moieties via a radical-free pathway, *ACS Catal.* 11 (2021) 9569–9577.
- [34] Y.-J. Zhang, G.-X. Huang, L.R. Winter, J.-J. Chen, L. Tian, S.-C. Mei, Z. Zhang, F. Chen, Z.-Y. Guo, R. Ji, Y.-Z. You, W.-W. Li, X.-W. Liu, H.-Q. Yu, M. Elimelech, Simultaneous nanocatalytic surface activation of pollutants and oxidants for highly efficient water decontamination, *Nat. Commun.* 13 (2022) 3005.
- [35] F. Ye, W. Sun, K. Pang, W. Yang, M. Pu, Q. Zhang, Coupling of sulfur and boron in carbonaceous material to strengthen persulfate activation for antibiotic degradation: active sites, mechanism, and toxicity assessment, *Chin. Chem. Lett.* 34 (2023), 107755.
- [36] L. Peng, X. Duan, Y. Shang, B. Gao, X. Xu, Engineered carbon supported single iron atom sites and iron clusters from Fe-rich enteromorpha for Fenton-like reactions via nonradical pathways, *Appl. Catal. B-Environ.* 287 (2021), 119963.
- [37] W.-D. Oh, T.-T. Lim, Graphene- and CNTs-based carbocatalysts in persulfates activation: material design and catalytic mechanisms, *Chem. Eng. J.* 354 (2018) 941–976.
- [38] Y. Yao, H. Chen, C. Lian, F. Wei, D. Zhang, G. Wu, B. Chen, S. Wang, Fe, Co, Ni nanocrystals encapsulated in nitrogen-doped carbon nanotubes as Fenton-like catalysts for organic pollutant removal, *J. Hazard. Mater.* 314 (2016) 129–139.
- [39] Y. Li, T. Yang, S. Qiu, W. Lin, J. Yan, S. Fan, Q. Zhou, Uniform N-coordinated single-atomic iron sites dispersed in porous carbon framework to activate PMS for efficient BPA degradation via high-valent iron-oxo species, *Chem. Eng. J.* 389 (2020), 124382.
- [40] B. Zhang, X. Li, K. Akiyama, P.A. Bingham, S. Kubuki, Elucidating the mechanistic origin of a spin state-dependent FeN_x-C catalyst toward organic contaminant oxidation via peroxymonosulfate activation, *Environ. Sci. Technol.* 56 (2022) 1321–1330.
- [41] N. Jiang, H. Xu, L. Wang, J. Jiang, T. Zhang, Nonradical oxidation of pollutants with single-atom-Fe(III)-activated persulfate: Fe(V) being the possible intermediate oxidant, *Environ. Sci. Technol.* 54 (2020) 14057–14065.
- [42] Y. Zou, J. Hu, B. Li, L. Lin, Y. Li, F. Liu, X. Li, Tailoring the coordination environment of cobalt in a single-atom catalyst through phosphorus doping for enhanced activation of peroxymonosulfate and thus efficient degradation of sulfadiazine, *Appl. Catal. B-Environ.* 312 (2022), 121408.
- [43] S.K. Han, T.-M. Hwang, Y. Yoon, J.-W. Kang, Evidence of singlet oxygen and hydroxyl radical formation in aqueous goethite suspension using spin-trapping electron paramagnetic resonance (EPR), *Chemosphere* 84 (2011) 1095–1101.
- [44] W. Zhang, B. Li, H. Ma, L. Zhang, Y. Guan, Y. Zhang, X. Zhang, P. Jing, S. Yue, Combining ruthenium (II) complexes with metal-organic frameworks to realize effective two-photon absorption for singlet oxygen generation, *Acs Appl. Mater. Interfaces* 8 (2016) 21465–21471.
- [45] C. Zhu, S. Zhao, Z. Fan, H. Wu, F. Liu, Z. Chen, A. Li, Confinement of CoP nanoparticles in nitrogen-doped yolk-shell porous carbon polyhedron for ultrafast catalytic oxidation, *Adv. Funct. Mater.* 30 (2020) 2003947.
- [46] X. Liang, D. Wang, Z. Zhao, T. Li, Y. Gao, C. Hu, Coordination number dependent catalytic activity of single-atom cobalt catalysts for Fenton-like reaction, *Adv. Funct. Mater.* 32 (2022) 2203001.
- [47] M. Feizbakhshan, B. Amdebrhan, Z. Hashisho, J.H. Phillips, D. Crompton, J. E. Anderson, M. Nichols, Effects of oxygen impurity and desorption temperature on heel build-up in activated carbon, *Chem. Eng. J.* 409 (2021), 128232.
- [48] A.M. Held, D.J. Halko, J.K. Hurst, Mechanisms of chlorine oxidation of hydrogen peroxide, *J. Am. Chem. Soc.* 100 (1978) 5732–5740.
- [49] S.J. Arnold, E.A. Ogryzlo, H. Witzke, Some new emission bands of molecular oxygen, *J. Chem. Phys.* 40 (1964) 1769–1770.
- [50] X. Lu, W. Qiu, J. Ma, H. Xu, D. Wang, H. Cheng, W. Zhang, X. He, The overestimated role of singlet oxygen for pollutants degradation in some non-photochemical systems, *Chem. Eng. J.* 401 (2020), 126128.
- [51] Y. Peng, H. Shi, Z. Wang, Y. Fu, Y. Liu, Kinetics and reaction mechanism of photochemical degradation of diclofenac by UV-activated peroxymonosulfate, *Rsc Adv.* 11 (2021) 6804–6817.
- [52] Y. Gao, Y. Rao, H. Ning, J. Chen, Q. Zeng, F. Tian, N. Gao, Comparative investigation of diclofenac degradation by Fe²⁺/chlorine and Fe²⁺/PMS processes, *Sep. Purif. Technol.* 297 (2022), 121555.
- [53] F. Han, X. Ye, Q. Chen, H. Long, Y. Rao, The oxidative degradation of diclofenac using the activation of peroxymonosulfate by BiFeO₃ microspheres—Kinetics, role of visible light and decay pathways, *Sep. Purif. Technol.* 232 (2020), 115967.
- [54] Z. Chen, S. He, M. Zhu, C. Wei, The effect of peroxymonosulfate in WS₂ nanosheets for the removal of diclofenac: information exposure and degradation pathway, *Chemosphere* 245 (2020), 125678.
- [55] H. He, J. Zhao, The efficient degradation of diclofenac by ferrate and peroxymonosulfate: performances, mechanisms, and toxicity assessment, *Environ. Sci. Pollut. Res.* 30 (2023) 11959–11977.
- [56] J. Peng, P. Zhou, H. Zhou, W. Liu, H. Zhang, C. Zhou, L. Lai, Z. Ao, S. Su, B. Lai, Insights into the electron-transfer mechanism of permanganate activation by graphite for enhanced oxidation of sulfamethoxazole, *Environ. Sci. Technol.* 55 (2021) 9189–9198.
- [57] N. Li, R. Li, X. Duan, B. Yan, W. Liu, Z. Cheng, G. Chen, L. Hou, S. Wang, Correlation of active sites to generated reactive species and degradation routes of organics in peroxymonosulfate activation by Co-loaded carbon, *Environ. Sci. Technol.* 55 (2021) 16163–16174.
- [58] K. Yin, Y. Shang, D. Chen, B. Gao, Q. Yue, X. Xu, Redox potentials of pollutants determining the dominate oxidation pathways in manganese single-atom catalyst (Mn-SAC)/peroxymonosulfate system: selective catalytic mechanisms for versatile pollutants, *Appl. Catal. B Environ.* 338 (2023), 123029.
- [59] X. Miao, X. Chen, W. Wu, D. Lin, K. Yang, Topological defects strengthened nonradical oxidation performance of biochar catalyzed peroxydisulfate system, *BIOCHAR* 5 (2023) 40.
- [60] H. Shi, G. Zhou, Y. Liu, Y. Fu, H. Wang, P. Wu, Kinetics and pathways of diclofenac degradation by heat-activated persulfate, *Rsc Adv.* 9 (2019) 31370–31377.
- [61] Z. Wang, H. Shi, S. Wang, Y. Liu, Y. Fu, Degradation of diclofenac by Fe (II)-activated peracetic acid, *Environ. Technol.* 42 (2021) 4333–4341.
- [62] R. Wang, H. Zhai, W. Luo, W. Liu, Z. Zhuang, M. Ji, Multifunctional sites on reduced graphene oxide synergistically improving the degradation of diclofenac in peroxydisulfate systems, *J. Environ. Chem. Eng.* 10 (2022), 108251.
- [63] S. Fergani, H. Hazoua, A. Saadi, S. Touati, A. Boudjemaa, K. Bachari, Activation of peroxymonosulfate by Co₂SnO₄/Co₃O₄/SnO₂ material for the effective degradation of diclofenac, *React. Kinet. Mech. Catal.* 136 (2023) 1033–1048.
- [64] J. Lee, U. Von Gunten, J.-H. Kim, Persulfate-based advanced oxidation: critical assessment of opportunities and roadblocks, *Environ. Sci. Technol.* 54 (2020) 3064–3081.